

Variations in the Galactic star formation rate and density thresholds for star formation

S. N. Longmore^{1*}, J. Bally², L. Testi^{1,3}, C. R. Purcell^{4,5}, A. J. Walsh⁶, E. Bressert^{1,7}, M. Pestalozzi⁸, S. Molinari⁸, J. Ott⁹, L. Cortese¹, C. Battersby², N. Murray¹⁰, E. Lee¹⁰, D. Kruijssen¹¹

¹European Southern Observatory, Karl-Schwarzschild-Strasse 2, D-85748 Garching bei München, Germany

²Center for Astrophysics and Space Astronomy, University of Colorado, UCB 389, Boulder, CO 80309

³INAF-Osservatorio Astrofisico di Arcetri, Largo E. Fermi 5, I-50125 Firenze, Italy

⁴School of Physics and Astronomy, University of Leeds, Leeds LS2 9JT, UK

⁵Sydney Institute for Astronomy (SiFA), School of Physics, The University of Sydney, NSW 2006, Australia

⁶Centre for Astronomy, School of Engineering and Physical Sciences, James Cook University, Townsville, QLD, 4811, Australia

⁷School of Physics, University of Exeter, Stocker Road, Exeter EX4 4QL

⁸INAF-Istituto Fisica Spazio Interplanetario, Via Fosso del Cavaliere 100, I-00133 Roma, Italy

⁹National Radio Astronomy Observatory, P.O. Box O, 1003 Lopezville Road, Socorro, NM 87801, USA

¹⁰Canadian Institute for Theoretical Astrophysics, 60 St. George Street, University of Toronto, Toronto, ON M5S 3H8, Canada

¹¹Max-Planck Institut für Astrophysik, Karl-Schwarzschild-Strasse 1, 85748, Garching, Germany

in prep.

ABSTRACT

The conversion of gas into stars is a fundamental process in astrophysics and cosmology. Stars are known to form from the gravitational collapse of dense clumps in interstellar molecular clouds, and it has been proposed that the resulting star formation rate is proportional to either the amount of mass above a threshold gas surface density, or the gas volume density. These star-formation prescriptions appear to hold in nearby molecular clouds in our Milky Way Galaxy’s disk as well as in distant galaxies where the star formation rates are often much larger. The inner 500 pc of our Galaxy, the Central Molecular Zone (CMZ), contains the largest concentration of dense, high-surface density molecular gas in the Milky Way, providing an environment where the validity of star-formation prescriptions can be tested. Here we show that by several measures, the current star formation rate in the CMZ is an order-of-magnitude lower than the rates predicted by the currently accepted prescriptions. In particular, the region $1^\circ < l < 3.5^\circ$, $|b| < 0.5^\circ$ contains $\sim 10^7 M_\odot$ of dense molecular gas — enough to form 1000 Orion-like clusters — but the present-day star formation rate within this gas is only equivalent to that in Orion. In addition to density, another property of molecular clouds, such as the amplitude of turbulent motions, must be included in the star-formation prescription to predict the star formation rate in a given mass of molecular gas.

Key words: stars:formation, ISM:evolution, radio lines:ISM, line:profiles, masers, stars:early type

1 INTRODUCTION

Stars play a pivotal role in shaping the cosmos. High-mass stars contributed to the ionisation of the Universe after the Cosmic Dark Ages. They drive energy cycles and chemical enrichment on galactic scales, hence sculpting galactic structure. Thus, the conversion of gas into stars is fundamental to astrophysics and cosmology.

The rate at which gas is converted into stars has been measured in the disks of nearby galaxies. When averaged over hundreds of parsecs, the star-formation rate (SFR) was found to have a power-law dependence on the gas surface-density as described by the Schmidt-Kennicutt (SK) relations (Schmidt 1959; Kennicutt 1998; Kennicutt & Evans 2012). A linear relationship is found between SFR and gas surface-density above a local extinction threshold, $A_K \sim 0.8$ magnitudes at a near-infrared wavelength of $2.2 \mu\text{m}$, corresponding to a gas column-density of $\sim 7.4 \times 10^{21} \mu\text{m}$.

* E-mail: slongmor@eso.org

hydrogen molecules per cm^{-2} or a gas surface-density Σ_{gas} , of $\sim 116 \text{ M}_{\odot}\text{pc}^{-2}$ (Lada et al. 2012). For a typical 0.1 pc radius cloud core, this corresponds to a volume density 3×10^4 hydrogen molecules cm^{-3} .

Alternatively, it has been proposed that the SFR density is linearly proportional to the mean gas density divided by the free-fall time multiplied by an efficiency factor estimated to be about 1% (Krumholz et al. 2012). These surface- and volume-density relations potentially unify our understanding of SFRs from the nearest star forming regions to ultra-luminous infrared galaxies (ULIRGs) and even star forming regions at intermediate to high redshifts (Swinbank et al. 2010; Danielson et al. 2011).

With the aim of testing these star formation (SF) scaling relations across large volumes of the Milky Way (MW), in § 2 we start by looking at the choice of observational diagnostics of dense gas and star formation activity in the Galaxy. In § 3, we present the survey data used in this work. In § 4 & 5 we discuss the striking differences between the dense gas and SF activity tracers across the Galaxy and investigate if any observational or systematic biases may be causing such differences. We find no evidence that the results are strongly affected by observational or systematic biases. In § 6 we then perform a quantitative analysis of the SFR and gas mass in the CMZ and directly compare this to predictions of proposed column density threshold and volumetric SF relations. In § 7 we summarise the results and discuss the implications for the universality of star formation relations.

2 OBSERVATIONAL DIAGNOSTICS OF DENSE GAS AND STAR FORMATION ACTIVITY IN THE MILKY WAY

We aim to test star formation scaling relations for representative samples of SF regions across large volumes of the MW. Such systematic studies are now possible thanks to the (near) completion of many blind, multi-wavelength, continuum and spectral line Galactic plane surveys. However, care must be taken in the choice of SF activity diagnostics. All surveys aiming to observe a large fraction of the dense gas in the Galaxy must look directly through the Galactic disk plane. Extinction therefore makes traditional UV, optical and even near-IR diagnostics of SF activity unusable for all but the closest regions. $24\mu\text{m}$ emission, commonly used to trace SF in extragalactic studies, suffers from extinction only in extreme environments (like the GC) but contamination from evolved stars can be significant, requiring other wavelength data to determine the source nature. Sensitivity and completeness limits mean counting young stellar objects still heavily embedded in their natal molecular clouds can only be done reliably for the closest SF regions.

Diagnostics are required at wavelengths longer than a few hundred microns, for which the Galaxy is effectively optically-thin. Sub-mm dust continuum emission is a robust gas mass tracer, but from this alone it is difficult to impose a volume density cutoff on the sample selection. Molecular line emission has the advantage that it can be used to probe gas within a certain density range. The actual density of gas probed by observations of a given transition is related to the critical density of that transition (the density at which the collisional de-excitation rate equals the Einstein A coefficient), but also depends non trivially on the sensitivity of the observations, the line opacity and gas kinetic temperature. A useful concept, taking into account these affects, is the effective critical density (Evans 1999). For a given transition, this is the density of gas probed by observations of a particular brightness temperature sensitivity for gas

at a given kinetic temperature. Assuming detected emission comes from gas at a similar kinetic temperature (a reasonable assumption for dense gas clumps in molecular clouds) and that beam dilution is not an issue, a uniform sensitivity molecular line transition survey offers a natural way to probe the amount of gas at, and above, the effective critical density.

Masers are well known indicators of SF activity and with strong transitions in the cm/mm wavelength regime they can be detected at large distances. However, it is not currently possible to derive an absolute star formation rate from first principles using masers. Free-free emission from ionised gas in HII regions created by young high mass stars is readily traced by cm-continuum and radio recombination line (RRL) emission, both of which are readily observable over large wavelength/frequency ranges (Peters et al. 2012). The number count of HII regions can give a handle on the relative numbers of SF sites across the Galaxy. The absolute star formation rate can be estimated from the luminosity of the cm-continuum emission by calculating the rate of ionising photons from high-mass stars (Murray & Rahman 2010), although contamination from non-thermal emission (which can lead to an overestimate of the SF activity) must be taken into account, especially towards the GC. It should be noted that each of these SF diagnostics traces the SF activity over different timescales. Masers are only observed towards regions that are still actively forming stars, so signpost SF activity on timescales of a few 10^5 yr. Free-free emission from HII regions is observed over the lifetimes of the high mass stars providing the ionising photons ie. timescales of a few Myr (Murray & Rahman 2010). When we refer to the SFR throughout this work, we are implicitly talking about star formation activity over these timescales, which is significantly shorter than other diagnostics (e.g. UV emission).

Of the recent and planned surveys¹, the H₂O Galactic Plane Survey (HOPS: Walsh et al. 2008, 2011; Purcell et al. 2012) is the only blind molecular line survey covering a large fraction (100 deg^2) of the Galactic plane simultaneously in multiple thermal molecular lines (including the important NH₃ molecule), masers and RRLs. Below we describe HOPS and several newly available Galactic plane surveys (see Table 1) which we use to investigate how the SFR relations and proposed density thresholds hold for more representative SF regions across the MW.

3 OBSERVATIONAL DATA

Determining the rate of SF per unit mass of gas requires measuring, i) the total gas mass and, ii) how much SF is taking place within this gas. We make use of recently available NH₃(1,1) data from HOPS and 70 to 500 μm data from the Herschel Infrared Galactic Plane Survey (HIGAL: Molinari et al. 2010) to trace the mass of dense gas across the Galaxy. Ammonia (NH₃) is well known as an excellent tracer of dense molecular gas at all evolutionary phases of the SF process (Ho & Townes 1983; Longmore et al. 2007; Beuther et al. 2009; Hill et al. 2010; Longmore et al. 2011), including the earliest phases where low temperatures mean molecules like CO freeze out on to dust grains and no longer reliably trace the gas. Given the HOPS sensitivity of 0.2 K we expect to detect gas with an effective critical density of a few 10^3 , probing gas close to, and above, the proposed volume density threshold (Evans 1999). The

¹ Although other large Galactic, molecular-line mapping projects are also being conducted on the Mopra telescope e.g. Barnes et al. (2011); Foster et al. (2011); Jones et al. (2012)

500 μm HiGAL data traces optically-thin dust emission, providing a measurement of the gas column density along a given line of sight. To directly compare the 500 μm and NH₃(1,1) emission, we first re-binned the 35'' 500 μm map to the HOPS pixel scale using Montage (<http://montage.ipac.caltech.edu/>), then applied the HOPS NH₃(1,1) emission mask to the re-binned HiGAL map. This provided the 500 μm emission from all HOPS NH₃ emission regions.

We use data from HOPS and the methanol multibeam (MMB Caswell et al. 2010, 2011; Green et al. 2010, 2012) surveys to detect the 22 GHz water maser emission and 6.7 GHz Class II methanol maser emission, respectively, across the Galactic plane. Both water and methanol masers are well known indicators of SF activity within molecular clouds. In particular, the 6.7 GHz Class II methanol maser transition is known to exclusively trace regions of high mass ($>8 \text{ M}_\odot$) (Minier et al. 2003)². Water masers are detected towards evolved stars, but these are found outside the disk-plane and the emission is typically two orders of magnitude weaker (Caswell et al. 2010). So sensitivity-limited, water maser Galactic plane surveys should predominantly trace SF regions. Removing evolved star contaminants is typically straightforward using other readily-available multi-wavelength data (Lumsden et al. 2002).

We use the radio recombination line (RRL) data from HOPS and the Green Bank Telescope (GBT) H_{II} Region Discovery Survey (HRDS; Anderson et al. 2011) to compare the Galactic H_{II} region number distribution to the dense gas and maser distributions. The HRDS completeness limit is sufficient to detect all H_{II} regions ionised by single O-stars to a distance of 12 kpc. Both HOPS and HRDS use RRLs to detect emission from H_{II} regions and the kinematic dimension helps to mitigate line-of-sight confusion that can affect continuum surveys. HRDS is much more sensitive than HOPS but is a targeted survey based on previous large-area cm-continuum and IR surveys. The HOPS RRL emission is less sensitive but allows for direct comparison with the maser, NH₃ and 500 μm data over the full 100 deg² of the HOPS survey region.

The H_{II} region number counts provide a measure of the relative distribution of SF sites across the Galaxy but we make use of recent analysis of WMAP data (Murray & Rahman 2010) to derive the absolute SFR in the GC.

4 COMPARING DENSE GAS EMISSION AND SF ACTIVITY TRACERS ACROSS THE GALAXY

As the Galaxy is optically-thin to the NH₃(1,1), 500 μm , water maser, methanol maser and RRL emission, the emission surface density ratios between these tracers in the plane of the sky is equivalent to that in a face-on view of the Galaxy. Comparing the emission ratios as a function of longitude and making the reasonable assumptions that i) the integrated intensity of the far-IR and NH₃(1,1) emission is proportional to the mass of dense gas, and, ii) the number of water masers, methanol masers, H_{II} regions and RRL integrated intensity is proportional to the amount of SF, we now investigate the relationship between the dense gas and SFR in the Galaxy.

Figure 1 shows the dense gas emission and current star formation activity tracers as a function of Galactic longitude (l) and latitude (b). The dense gas distribution is dominated by the very

bright and spatially-extended emission within a few degrees of the Galactic centre – the CMZ (Morris & Serabyn 1996; Ferrière et al. 2007). This is easily distinguished from the rest of the Galactic plane by the very high intensity of dense gas emission and large gas velocity dispersion as indicated by wide spectral lines. While the dense gas emission is highly concentrated in the CMZ, the distribution of star formation activity tracers is relatively uniform across the Galaxy. Quantitatively, the CMZ accounts for $\sim 80\%$ of the integrated NH₃(1,1) intensity but only contains 4% of the survey area. Yet, the CMZ does not stand out in either water or methanol maser emission, or in the number of H_{II} regions, which all trace recent high-mass star formation. A qualitatively similar trend is reported by Beuther et al. (2012) who compare the sub-mm dust continuum emission and GLIMPSE point sources as a function of Galactic longitude.

Figure 2 shows Galactic longitude distributions of dense gas and star-formation activity indicators summed over the observed latitude range ($-0.5^\circ \leq b \leq 0.5^\circ$) for each longitude pixel. To make a direct comparison of dense gas and SF tracers as a function of longitude, we first sampled in 2-degree longitude bins to ensure the volume of the Galaxy covered in each bin contains a large number of SF regions and so is appropriate for testing SF relations (Onodera et al. 2010). The emission or number count in each 2 degree longitude bin was then normalised by the total emission or number in the full survey area.

The top panel of Figure 3 shows that there is a strong correlation between independent dense gas tracers. To separate the CMZ emission from that in the rest of the Milky Way, from here on we refer to the region $|l| < 5^\circ$ with NH₃(1,1) line widths $\Delta V > 15 \text{ kms}^{-1}$ as “GC-only”, to distinguish it from the rest of the Galaxy, which we refer to as the “non-GC” region. No offset is seen in the correlation between the GC-only and non-GC regions. The middle panel of Figure 3 shows a correlation between the dense gas and SF tracers for the non-GC regions. However, the GC-only regions are clearly distinct, with at least an order of magnitude brighter dense gas emission for the number of SF activity tracers.

The bottom panel of Figure 3 shows the resulting dense gas vs SF tracer surface density ratio in Galacto-centric radius, R_{GC} , annuli of 0.5 kpc. R_{GC} was calculated using the Galactic rotation curve of Brand & Blitz (1993) and assuming a distance to the Galactic centre of 8.5 kpc and a solar velocity of 220 km s^{-1} . The gas between the CMZ and $R_{\text{GC}} \sim 3$ kpc shows emission at anomalous velocities so the rotation curve does not place reliable constraints on R_{GC} over this range. The surface density ratios over this region, highlighted by the hatched rectangle, should be ignored. The ratio is approximately constant at $R_{\text{GC}} > 3$ kpc. This suggests the linear relationship observed between the quantity of gas above the proposed extinction threshold and the SFR (Gao & Solomon 2004; Wu et al. 2005; Lada et al. 2012) extends to a larger number of more representative SF regions across the Galaxy. By comparison, the dense gas surface density towards the GC ($R_{\text{GC}} < 0.5$ kpc) is orders of magnitude too large compared to the SF activity surface density.

5 VARIATION IN SFR PER UNIT MASS OF DENSE GAS BETWEEN THE DISK AND GALACTIC CENTRE?

We now investigate the striking difference between the longitude and surface density distribution of dense gas and SF tracers between the GC-only and non-GC regions (Figure 3). If the number

² Although the origin of the masers in disks or outflows is debated (e.g. Norris et al. 1998; Minier et al. 2000; De Buizer et al. 2009, 2012).

of masers and H_{II} regions were directly proportional to the integrated intensity of the dense gas emission, as would be expected if assumptions i) and ii) outlined in § 4 hold, and the SFR was set by the amount of dense gas, how many would be expected towards the GC-only region? With $\sim 1/25$ of the HOPS survey area and 4 times the total NH₃(1,1) integrated intensity outside the GC, the GC-only region has ~ 100 times the dense gas integrated intensity per unit survey area compared to the non-GC region. Therefore, the expected number of masers and H_{II} regions towards the GC should also be 100 times larger per unit area. The SF activity per unit area as traced by methanol masers is a factor 3 to 6 higher in the inner 250 pc of the Galaxy compared to the spiral arms (Caswell et al. 2010). However, our results show that this increase in maser surface density is dwarfed by the increase in the dense gas surface density. Given the amount of dense gas, the GC-only region appears deficient in SF tracers by two orders of magnitude. Taken at face value this suggests large differences in SFR per unit mass of dense gas between the disk and Galactic centre. Below we investigate if such a large deficit could be caused by observational or systematic biases affecting the emission from one or more of the tracers used in this study.

5.1 Potential observational biases

These data are from blind large-area surveys with approximately uniform sensitivity. Therefore, the results should not be affected by target selection criteria or variable sensitivity. But what about the sensitivity limits themselves? For example, could HOPS be missing a large fraction of the dense molecular gas outside the GC-only region as this NH₃(1,1) emission falls beneath the sensitivity threshold? Purcell et al. (2012) show HOPS should detect 400 M_⊙ clumps to 5.1 kpc and 5000 M_⊙ clumps to the Galactic centre distance. These limits suggest completeness is not a problem.

Alternatively, as the GC-only clouds are more distant on average than the non-GC regions, could there be a large number of weak water masers towards the GC-only region which fall below the HOPS detection limit? Ott et al (in prep.) have mapped the entire CMZ from 20 to 28 GHz with Mopra in a similar setup to the HOPS observations but with $\sim 8\times$ better sensitivity and using the correlator in broadband rather than zoom mode (resulting in velocity resolution of 3.5 km s⁻¹ rather than 0.4 km s⁻¹ as for HOPS). They find approximately twice the number of masers – not enough to account for the apparent deficit.

Sites of maser emission observed with a single dish may be resolved into multiple sites when observed at higher angular resolution with an interferometer. This will not affect the methanol masers counts as they all have interferometric follow-up, but may affect the HOPS water maser distribution. To investigate this, we compared the HOPS detections to $\sim 4\times$ deeper, interferometric water maser observations toward a 0.5 deg² region surrounding the GC (Caswell et al. 2011). In the same region ($|l|, |b| < 0.4^\circ$), 27 masers were found compared to the 8 found by HOPS, and 3 of the 8 HOPS detections were resolved into 2 maser sites. If this is representative of the whole GC-only region HOPS may have underestimated the number of water masers by a factor of 3. Preliminary results from a deeper, interferometric EVLA water maser survey covering $|l| < 1.5^\circ, |b| < 1^\circ$ also recover a similar factor of 3 increase in number of detections compared to HOPS over the same region (J. Ott, F. Yusef-Zadeh private communication). This is not sufficient to explain the large disparity between the maser and dense gas distributions in the GC-only and non-GC regions. Just as importantly, there is also no reason to expect a systematic difference

between the number of maser sites each HOPS detection will be resolved into between the GC and non-GC regions. This is confirmed by preliminary results from the interferometric follow-up observations of the HOPS masers (Walsh et al, in prep). As a further check, repeating the analysis using the integrated intensity of the masers (which will not be affected by how many maser sites each HOPS detection is resolved into at higher resolution), rather than number of masers, as a function of longitude produces the same results in Figures 2 & 3. We adopt a conservative factor of 3 uncertainty in the maser counts, which we illustrate by the error bar in the middle panel of Figure 3. The similarity of both maser distributions in the bottom panel of Figure 3 gives confidence in the robustness of the maser counts and the adopted uncertainty.

Finally, the trends in Figure 3 consist of ratios between observed parameters rather than the absolute values of the parameters themselves. The distance-dependence on expected source flux is the same for all observed parameters, so the trend itself will not be affected by systematic differences in distance between the GC-only and non-GC regions. We conclude that there is no evidence that our results may be strongly affected by observational biases.

5.2 Potential systematic biases in the dense gas and SF tracers

Many mechanisms can affect assumption i) above, the most important of these being: the emission optical depth (assumed to be optically-thin); ammonia abundance and gas excitation conditions; dust properties (composition, temperature) and gas-to-dust ratio. These properties will certainly vary from one molecular cloud to another and undoubtedly cause much of the scatter seen in Figure 3 as well as the non-linear slope in the NH₃(1,1) integrated intensity vs 500 μm flux. The variation in these properties must be understood before interpreting differences between individual clouds or deriving physical properties of the gas directly from one of these tracers. However, we are averaging over many molecular cloud complexes and are interested in order-of-magnitude variations across the Galaxy so focus on systematic differences between GC-only and non-GC regions.

5.2.1 Potential systematic biases in the dense gas mass estimates

Regarding the mass estimates, the emission optical depth will on average likely be much higher towards the GC-only regions, leading to a substantial underestimate of the dense gas mass towards the GC. This only accentuates the difference between the Galactic centre and the rest of the Galaxy. However, many observations show the GC excitation conditions and dust temperature are on average higher. The most relevant temperature measurements for this work are those derived directly from NH₃. Targeted observations of multiple NH₃ inversion transitions towards GC GMCs show these have at least two kinetic temperature regimes – a cool (25 K) component which dominates the column density and a warm (200 K) component which accounts for $\sim 25\%$ of the column density (Huettemeister et al. 1993). Beam-averaged temperature measurements at the HOPS resolution results in an average T_K of ~ 50 K for GC clouds (J. Ott, priv comm.). Compared to ~ 20 K for typical GMCs, this would lead to an overestimate of the GC dense gas mass by a factor 2 – 3.

As the average gas kinetic temperature is higher in the GC, the NH₃(1,1) effective critical density will be lower. Given the uniform sensitivity of the HOPS observations, this means the GC NH₃(1,1)

integrated intensity will include emission from lower density gas. As the ultimate goal is to compare the amount of gas across the Galaxy above a single density threshold, including lower density material will lead to a systematic overestimate of this value towards the GC. The magnitude of the overestimate will depend on both the difference between the effective critical density probed towards the GC and the rest of the Galaxy, and how much additional gas in the GC lies between these two effective critical density limits. The NH₃(1,1) effective critical density changes by less than a factor 2 for gas with kinetic temperatures between 10 K and 100 K (Evans 1999). The line brightness temperature of 1 K used in these calculations corresponds to 5 times the HOPS r.m.s. sensitivity so is a sensible limit. As the average gas kinetic temperature difference between the GC and the Galaxy is much less than this (see above), the effective critical density probed will be very similar. In § 6 we estimate the average density of gas in the CMZ to be $\sim 5 \times 10^3 \text{ cm}^{-3}$, so most of the gas will be close to or above the effective critical density. We conclude systematic differences in the effective critical density probed between the GC-only and non-GC regions will not affect the result.

Extrapolating the observed metallicity gradient in the disk of -0.03 to $-0.07 \text{ dex kpc}^{-1}$ (Balser et al. 2011), one would expect the metallicity to increase by a factor 3–4 from the sun to the Galactic centre. While some studies do find an increased metallicity towards the Galactic centre, others find close to solar values (Shields & Ferland 1994; Najarro et al. 2009). Using the commonly adopted assumption that the Galactic centre metallicity is twice solar (Ferrière et al. 2007), the gas-to-dust ratio in the Galactic centre is likely lower by the same value. This means the 500 μm flux towards the Galactic centre systematically over-estimates the dense gas mass by a factor ~ 2 compared to the disk. Similarly, the NH₃ abundance gradient in the disk (Dunham et al. 2011) implies an average factor ~ 2 relative overestimate in the Galactic centre NH₃-derived mass estimate. Both the 500 μm and NH₃ dense gas mass estimates therefore over-predict the Galactic centre mass by a factor ~ 2 . No systematic effects are known regarding dust composition with Galacto-centric radius.

Another potential worry is related to beam dilution. The NH₃(1,1) emission from the GC covers a large angular area on the sky and thus fills the 2' beam of the HOPS observations. If the molecular clouds outside of the GC systematically had angular sizes much smaller than the 2' beam, the measured NH₃(1,1) surface brightness would be affected by beam dilution and the integrated intensity would be systematically underestimated. To assess whether this effect is important, we estimated the distance at which molecular clouds of a given mass will be the same angular size as the 2' HOPS beam. The physical radius as a function of mass was estimated using the Kauffmann & Pillai (2010) empirical mass-size relationship, $M = 870M_{\odot}(r/\text{pc})^{1.33}$, for molecular clouds which will proceed to form high mass stars. Based on this relation, the line in the top panel of Figure 6 shows the distance at which a molecular cloud of a given mass will have an angular size of 2'. Molecular clouds below the line will suffer from beam dilution so the observed surface brightness will be reduced, and the integrated intensity underestimated. From this we conclude that beam dilution is undoubtedly an important factor for low-mass clouds at large distances. An implicit assumption in the above analysis is that it is possible to detect the emission from all the gas in the cloud. However, the density fluctuations in molecular clouds mean that some of the gas may lie at low density and not excite NH₃ emission. We can estimate the effect of this by calculating the average density of the gas inferred from the empirical mass-size relation (Kauffmann & Pillai 2010),

$n(H_2) = 3.13 \times 10^3(r/\text{pc})^{-1.67} \text{ cm}^{-3}$. As shown in the bottom panel of Figure 6, clouds up to $\sim 1000 M_{\odot}$ have average volume densities several 10^3 cm^{-3} and above, so we would expect most of the gas to emit in NH₃. The average density of more massive clouds drops, so the fraction of NH₃ emitting gas will drop too. Although the top panel of Figure 6 shows HOPS will easily resolve very massive clouds to large distances, the NH₃ emission must come from denser clumps within these clouds. The extent to which beam dilution affects the detected NH₃ emission, if at all, depends on the density fluctuations within the clouds, which will vary from cloud to cloud. However, the fact that in general the larger the cloud, the better it will be resolved, mitigates the fact that less of the gas will be at high density. We conclude that while beam dilution undoubtedly affects low-mass clouds at large distances, it is not an important issue for clouds of a thousand solar masses and greater. It is the clouds in this mass regime that will be forming the high-mass stars traced by methanol maser emission and HII regions.

On balance, the systematic effects would argue that making assumption i) would overestimate the dense gas mass towards the GC relative to the rest of the Galaxy. However, it seems highly unlikely these would lead to an overestimate by a factor of ~ 100 . Additionally, as most of these effects are (at least partially) independent between the 500 μm and ammonia emission, the fact that no jump is seen in the correlation between the two tracers in Figure 3 when comparing the GC-only and non-GC regions argues the systematics are not important for the analysis presented here. Based on the above arguments and the observed scatter in the 500 μm vs ammonia emission correlation (top panel of Figure 3), we adopt a factor 5 uncertainty, which is illustrated by the error bars in Figure 3.

5.2.2 Potential systematic biases in the maser counts

As water masers are also observed towards evolved stars, contamination may affect the maser number counts. As previously stated, the water masers from evolved stars are found outside the disk-plane and the emission is typically two orders of magnitude weaker (Caswell et al. 2010). Therefore, sensitivity-limited, water maser Galactic plane surveys should predominantly trace SF regions. Nevertheless, we are conducting high angular resolution follow-up observations of the HOPS masers to uncover the true nature of each maser detection. Preliminary results show the majority ($\sim 70\%$) are associated with SF. Also, no trends in the relative number of masers associated with evolved stars or SF regions are seen with Galactic longitude (Walsh et al., in prep.). In any case, if anything, one might expect more evolved stars towards the bulge and Galactic centre. Contamination of water masers from evolved stars would lead to an *increase* in number of water masers observed towards the GC. This only strengthens the result. Finally, the similarity of the water maser distribution in the bottom panel of Figure 3 to the methanol maser distribution (which are not observed towards evolved stars), adds further weight that contamination does not affect the results.

Given the tight constraints on the physical conditions required for masers to exist, another possibility is that maser emission is somehow quenched towards the Galactic centre region. This seems plausible given the extreme environmental conditions in the Galactic centre compared to the rest of the disk (e.g. interstellar radiation field enhanced by 10^3 , external pressure $P/k \sim 10^8$, strong magnetic fields, turbulence, gamma rays: Morris & Serabyn 1996; Ferrière et al. 2007; Crocker et al. 2010). However, masers are formed deeply embedded within GMCs so they are shielded from the interstellar radiation field. Regarding the effect of turbu-

lence, the coherence path lengths for masers are of order AU size scales, so individual maser emission regions will not be affected by velocity flows or gas kinematics on pc-scales (Mark Reid, private communication). Additionally, extremely bright “mega masers” are known to exist in the circumnuclear disks around supermassive black holes – an even more extreme environment than the CMZ. It is worth pointing out that the pumping mechanisms for water and methanol masers are different. As far as we are aware, no known effect in maser pumping theory can account for the observed factor 100 deficit in the number of both water and methanol masers towards the GC-only region. We conclude there is no evidence that our results are strongly affected by systematic biases in the dense gas and SF tracers.

6 QUANTITATIVE ANALYSIS OF THE SFR AND GAS MASS IN THE CMZ

The previous qualitative analysis strongly points to large differences between the SFR per unit mass of dense gas in the CMZ and the rest of the Galaxy. However, the inability to derive absolute SFRs from first principle for masers and the large uncertainties in deriving masses from $\text{NH}_3(1,1)$ integrated intensities preclude us from a more quantitative analysis using these tracers. Therefore, we now focus on the CMZ, the region which stands out as potentially discrepant, and aim to directly test the predictions of different SF relations.

6.1 Structure and physical properties of the molecular gas in the Galactic centre

The Galactic centre environment has been well studied (Morris & Serabyn 1996; Ferrière et al. 2007). Here we summarise the structure and physical properties of the molecular gas within a Galacto-centric radius (r_{GC}) of 500 pc ($|l| < 3.5^\circ$) – ie the central molecular zone (CMZ). The CMZ can be decomposed into an outer and inner component, separated at $r_{GC} \sim 230$ pc, and further separated the inner CMZ into a “disk” and torus, with approximate radial ranges of 0 to 120 pc and 130 to 230 pc, respectively (Launhardt et al. 2002). Based on the far-IR dust continuum emission (Launhardt et al. 2002), the mass of the disk and torus components are derived to be $\sim 4 \times 10^6 \text{ M}_\odot$ and $\sim 1.6 \times 10^7 \text{ M}_\odot$, respectively, with a total CMZ mass ($r_{GC} \leq 500$ pc) of $\sim 6 \times 10^7 \text{ M}_\odot$. Despite the many systematic uncertainties in dust-derived masses, and the notoriously uncertain X-factor affecting CO-derived mass estimates, there is general agreement in the literature that the total molecular gas mass within $r_{GC} \leq 500$ pc is $2 - 6 \times 10^7 \text{ M}_\odot$ (Ferrière et al. 2007).

Numerous studies have argued for two distinct molecular gas components: a warmer, low-density component ($\leq 10^3 \text{ cm}^{-3}$) of “diffuse” clouds with a large filling factor and comprising $\sim 30\%$ of the mass, and a high-density ($\geq 10^4 \text{ cm}^{-3}$) component with a volume filling factor of roughly a few percent (see Ferrière et al. 2007, for details). Given the effective critical density of the $\text{NH}_3(1,1)$, it is likely the HOPS observations are tracing the dense component.

The recent far-IR HiGAL survey provides a new, high angular resolution view of the CMZ molecular gas properties (Molinari et al. 2011). We derive the column density maps for the region $-2.5^\circ < l < 3.5^\circ$, $|b| \leq 0.5^\circ$ using well-tested methods (Battersby et al. 2011). A major systematic uncertainty is the assumed dust opacity and we note that we systematically underestimates the mass by a factor 2–3 compared to the DUSTEM method

(e.g. Molinari et al. 2011) for this reason. Figure 4 shows the total mass of gas which lies above a range of different column density thresholds. The different curves show the effect on the derived column density of using different wavelength bands and different source-extraction algorithms. From this we conclude the mass derived from the column densities to be robust to the background and source extraction to the 10–20% level.

The vertical lines in Figure 4 show the Lada et al. (2012) proposed column density threshold of $7.5 \times 10^{21} \text{ cm}^{-2}$, calculated from the Lada et al. (2012) extinction threshold of $A_V = 8$ mag and assuming an $A_V \rightarrow N_{H_2}$ conversion of $N_{H_2} = A_V \times 0.95 \times 10^{21} \text{ cm}^{-2}$ (Frerking et al. 1982). This shows that most of the mass in this region lies above an extinction of $A_V = 8$ mag. The masses derived from this analysis are reported in Table 2. The total derived mass of the CMZ gas from the HiGAL data is $4.1 \times 10^7 \text{ M}_\odot$, in good agreement with previous measurements in the literature (Ferrière et al. 2007).

Determining the volume density of the gas from the HiGAL column density maps is not straightforward as it depends on knowledge of the 3D gas structure. For the most part this is not well constrained towards the Galactic centre. The region of the CMZ with the best quantified 3D structure is the molecular torus, or “100 pc ring” (Molinari et al. 2011). The volume of gas in a ring of radius R and width ΔR , with a thickness of H , is

$$V = 2\pi R \Delta R H = 4.4 \times 10^{60} \left(\frac{R}{100 \text{ pc}} \right) \left(\frac{\Delta R}{12 \text{ pc}} \right) \left(\frac{H}{20 \text{ pc}} \right) \text{ cm}^{-3} \quad (1)$$

The fiducial radius of 100 pc is that determined for the ring and the fiducial width of 12 pc is based on the observed column density maps (Molinari et al. 2011). We have used $H = 20$ pc assuming hydrostatic equilibrium ($H/R = v_T/v_c$); the circular velocity $v_c \approx 100 \text{ km s}^{-1}$ while the turbulent velocity $v_T \equiv \sqrt{8 \ln 2} \sigma_v = 20 \text{ km s}^{-1}$ (Oka et al. 2001).

With a mass of $1.8 \times 10^7 \text{ M}_\odot$ (see column 5 of Table 2), the volume density for the ring is then

$$n = \frac{M_g}{m_p V} \approx 5000 \left(\frac{R}{100 \text{ pc}} \right)^{-1} \left(\frac{\Delta R}{12 \text{ pc}} \right)^{-1} \left(\frac{H}{20 \text{ pc}} \right)^{-1} \text{ cm}^{-3}. \quad (2)$$

Note that this mass is a factor ~ 1.7 smaller than reported previously (Molinari et al. 2011) due to the different dust opacities used in that work. The inferred densities in this work are therefore also lower by the same factor. The surface density of the ring is

$$\Sigma_{ring} = \frac{M_g}{2\pi R \Delta R} \approx 2400 \left(\frac{R}{100 \text{ pc}} \right) \left(\frac{\Delta R}{12 \text{ pc}} \right) \text{ M}_\odot \text{ pc}^{-2}, \quad (3)$$

or

$$\Sigma_{ring} = 0.5 \text{ g cm}^{-2}. \quad (4)$$

As the gas in the ring is observed to be clumpy, the density at individual positions along the ring may clearly deviate from these representative values.

The gas in the ring has been modelled as a twisted ellipse with semi-major and semi-minor axes of 100 pc and 60 pc, respectively (Molinari et al. 2011). The dashed vertical lines in Figure 5 show the average volume density assuming the ellipse has the average cylindrical diameter (ie $H = \Delta R$) specified by the annotated values. From the measured height of the ring projected on the plane of the sky we estimate the average volume density to be $\sim 5 \times 10^3 \text{ cm}^{-3}$. This agrees well with the analytical estimate

above and also volume densities estimated by previous authors for the dense component of the CMZ molecular gas (see above).

We note that the gas volume density and interpretation of the measured column density changes considerably if the gas structure is different than assumed above. For example, in the worst-case scenario, if the gas assumed to make up the ring actually lay in a uniform disk with the same radius, the volume density would drop to around a few 10^2 cm^{-3} . Additionally, the measured column density would be highly dependent on the viewing angle, and appear much larger if viewed through the disk-plane rather than in a face-on view of the Galaxy. In this case it would not be fair to test the predictions of the column density threshold SF relations using the directly measured column density without taking this into account.

However, several lines of evidence suggest this is not the case. On top of the modelling which successfully reproduces the gas kinematic structure (Molinari et al. 2011), analysis of emission from many high critical density molecular line transitions show the majority of the gas in the CMZ is cold, has a density $\gtrsim 10^4 \text{ cm}^{-3}$ and a volume filling factor of only a few percent. In addition, if the gas was uniformly distributed, one would expect optically thin emission (e.g. from sub-mm dust emission) to peak along the line of sight with the largest path length, i.e. directly through the centre. In fact the emission intensity increases towards the edges, directly contradicting what would be expected from a uniform disk, and as expected from the emission arising in a ring.

6.2 Measured CMZ SFR values

Values of the SFR for the CMZ in the literature vary by factors of several, but recent measurements based on number counts of massive young stellar objects, appear to converge to a value close to $0.1 M_{\odot} \text{ yr}^{-1}$ (e.g. $0.14 M_{\odot} \text{ yr}^{-1}$ and $0.08 M_{\odot} \text{ yr}^{-1}$: Yusef-Zadeh et al. 2009; Immer et al. 2012).

As an alternative approach, we make use of the recent analysis of WMAP data (Murray & Rahman 2010) to determine the fraction of ionising photons in the Galaxy coming from the GC. This analysis offers many advantages over older estimates of the ionising photon flux. WMAP has much better absolute flux precision, suffers less from spatial filtering and observed at multiple frequencies so the spectral index of the emission can be calculated allowing the relative contributions from free-free, non-thermal and spinning dust emission to be determined. Although the WMAP beam is large, $\sim 1^\circ$ at the lowest frequencies, the free-free emission in the Galaxy is dominated by the so-called “extended low density” (ELD) H α emission, rather than classical H α regions (Murray & Rahman 2010).

Based on the free-free-only contribution to the 33 GHz flux, corrected for dust attenuation, the rate of ionising photons, Q , across the Galaxy is measured to be $2.9 \times 10^{53} \text{ s}^{-1}$ (Lee et al. 2012). The SFR, \dot{M}_* , is then given by (Murray & Rahman 2010)

$$\dot{M}_* = Q \frac{\langle m_* \rangle}{\langle q \rangle} \frac{1}{\langle t_Q \rangle}, \quad (5)$$

where $\langle q \rangle$ is the ionising flux per star averaged over the stellar initial mass function and $\langle m_* \rangle$ is the mean mass per star. The quantity $\langle t_Q \rangle$ is the ionisation-weighted stellar lifetime, or time at which the ionising flux of a star falls to half its maximum value, averaged over

the IMF³. Murray & Rahman (2010) show that

$$\frac{\langle m_* \rangle}{\langle q \rangle} = 1.59 \times 10^{-47} M_{\odot} \text{ s} \quad (6)$$

and

$$\langle t_Q \rangle = 3.9 \times 10^6 \text{ yr}. \quad (7)$$

The reason this timescale is small compared to the average lifetime of stars in a cluster is because $\langle t_Q \rangle$ is dominated by stars $> 40 M_{\odot}$ (Murray 2011). While stars of $> 8 M_{\odot}$ (with lifetimes significantly longer than $\langle t_Q \rangle$) produce ionising photons, the main-sequence life time of stars $> 40 M_{\odot}$ is a slowly varying function of mass, while the ionising photon output continues to increase rapidly. The WMAP observations are therefore sensitive to star formation over the last ~ 4 Myr.

From the total rate of Lyman continuum photons in the Galaxy of $Q = 2.9 \times 10^{53} \text{ s}^{-1}$, the total SFR is calculated to be $1.3 M_{\odot} \text{ yr}^{-1}$ (Murray & Rahman 2010). In Table 2 we show the Q values for the same latitude and longitude regions as the previous gas mass calculations. The range of values in column 7 show the total Q assuming the near and far kinematic distances. Column 9 gives the fraction of the total Galactic Q that the average of these values corresponds to. Based on this analysis, for the latitude range of $|b| < 0.5^\circ$, the longitude ranges $-2.5^\circ < l < -1.0^\circ$, $|l| < 1^\circ$ and $1^\circ < l < 3.5^\circ$ therefore have SFRs of ~ 0.016 , ~ 0.015 and $\sim 0.0036 M_{\odot} \text{ yr}^{-1}$, respectively. We report these numbers in Table 2.

This means that in total $\sim 2.8\%$ of the star formation in the Galaxy lie in this l and b range. Although this encompasses the region most people would use to define the CMZ, given the different angular resolutions of the studies used to derive the mass and SFR, we check to make sure the hard l and b boundary imposed is not affecting this result. The WMAP data extend to higher latitudes, and we note that including the latitude range $|b| < 1^\circ$ for the $|l| < 1^\circ$ region increases the maximum Q by a factor ~ 3 . The total SFR over this larger region is $0.06 M_{\odot} \text{ yr}^{-1}$. The Q values over the larger latitude range are shown in parentheses in columns 7, 9 and 10 of Table 2. The other longitude regions are not affected by increasing the latitude range. As a final check, we note that the total Q in the much larger region $|l| < 4^\circ$, $|b| < 1^\circ$ is 1.64×10^{52} , corresponding to 5.6% of the total Galactic SFR.

6.3 Comparing measured CMZ gas mass and SFRs with those predicted from SF relations

We now compare the measured gas mass and SFRs determined for the CMZ above, with the values predicted from the column-density threshold and volumetric SF relations.

6.3.1 Column-density threshold SF relation: predicted CMZ SFR

The Lada et al. (2012) column-density threshold relation proposes the SFR in a molecular cloud is set by the amount of gas above a column density threshold corresponding to an extinction of $A_V = 8 \text{ mag}$. This is parametrised through, $SFR = 4.6 \times$

³ Assuming high mass stars are well selected from the IMF as expected if their formation is intrinsically linked with the formation of massive stellar clusters (e.g. Smith et al. 2009). However, this assumption may be affected if stochastic sampling of the IMF is important (see e.g. Bressert et al. 2012).

$10^{-8}(f_D) M_{\text{gas}}(M_\odot) \text{M}_\odot \text{yr}^{-1}$, where the factor f_D is the fraction of the total gas mass (M_{gas}) above the column density threshold. Table 2 shows the mass of gas above the column density threshold for the three different CMZ regions. Based on these mass measurements, the predicted SFRs for these regions are 0.18, 0.78 and $0.74 \text{ M}_\odot \text{yr}^{-1}$. These values are listed in column 11 of Table 2.

6.3.2 Volumetric SF relation: predicted CMZ SFR

Next we consider the Krumholz et al. (2012) volumetric star formation relation which is parametrised through:

$$\frac{\text{SFR}}{[\text{volume}]} = \eta \frac{M_{\text{mol}}}{[\text{volume}]} \frac{1}{\tau_{\text{ff}}} = 0.01 \frac{M_{\text{mol}}}{[\text{volume}]} \frac{1}{\tau_{\text{ff}}} \quad (8)$$

where the SFR in a given volume of gas per free-fall time (τ_{ff}) is determined by the mass of the molecular gas (M_{mol}) in that volume and a global efficiency of gas converted to stars per free-fall time, η , of 1%. The free-fall time is

$$\tau_{\text{ff}} \equiv \sqrt{\frac{3\pi}{32G\rho}} = 3.6 \times 10^5 \left(\frac{10^4 \text{ cm}^{-3}}{n} \right)^{1/2} \text{ yr}. \quad (9)$$

The free-fall time, and hence gas density, for the gas in the GC clearly plays an important role in setting the predicted SFR. As discussed in § 6.1, the region of the CMZ with the best constrained gas structure is the 100 pc ring (see § 6.1). From Eq 8 & 9, the SFR predicted by the volumetric relation is given by,

$$\dot{M}_* = \eta M_g / \tau_{\text{ff}} = 0.53 \left(\frac{n}{8000 \text{ cm}^{-3}} \right)^{1/2} M_\odot \text{yr}^{-1}, \quad (10)$$

for $\eta = 0.01$. This is twenty times the observed star formation rate. The fiducial predicted SFR increases to $0.9 \text{ M}_\odot \text{yr}^{-1}$ for $\eta = 0.017$ (e.g. Kennicutt 1998).

Given the clumpy nature of the gas in the ring, for illustrative purposes, Figure 5 plots the predicted SFR as a function of the gas density. The dashed lines show the range in observed thickness (Molinari et al. 2011), or scale height H (and hence the inferred radial extent ΔR if the ring is cylindrical) of the ring from $\sim 6 \text{ pc}$ to factors of several larger.

We note that, if instead of using the observed geometry of gas, one assumes the GC gas mass is spread over a uniform disk of diameter $\sim 100 \text{ pc}$, the expected free-fall time significantly increases, and the predicted star formation rate drops considerably. Using this much larger free-fall time might be appropriate if the timescale for star formation in the GC was set by the time it would take the gas to collapse to the centre of the ring. However, the observed gas dynamics show that the ring is not collapsing towards the centre, but rather rotating around the centre of the ring (Molinari et al. 2011). In addition the gas in the ring clearly fragments, and the free-fall time at the observed local density is much shorter than the time it would take to collapse to the centre (assuming no rotational support). We conclude that the observed local volume density of $\sim 5 - 8 \times 10^3 \text{ cm}^{-3}$ is the correct density to use for the purpose of calculating the free-fall time.

We believe the reason our results contradict previous authors who have concluded the CMZ lies on the S-K relation (e.g. Yusef-Zadeh et al. 2009; Kennicutt & Evans 2012) is because they assumed the observed CMZ gas lay in a uniform disk and thus had a much lower average volume density.

Assuming the rest of the gas in the outer CMZ is at a similar density to that in the torus (Ferrière et al. 2007), the predicted SFR for the $-3.5^\circ < l < -1^\circ$ and $1^\circ < l < 2.5^\circ$ regions are 0.14 and

$0.39 \text{ M}_\odot \text{yr}^{-1}$, respectively. The predicted SFR values are listed in column 12 of Table 2.

6.3.3 Predicted vs measured SFR values

The predicted SFRs in Table 2 for both the column density threshold and volumetric SF relations agree to within a factor of two. The measured SFRs are at least a factor 10 smaller than the predicted values for all three regions. The region of the outer CMZ at positive longitudes (ie $1^\circ < l < 3.5^\circ$) stands out as extreme in this regard. Despite containing almost the same reservoir of gas as the inner CMZ (ie $|l| < 1^\circ$), it has a much lower measured SFR. Both the column density threshold and volumetric SF relations over-predict the SFR in this region by two orders of magnitude.

However, the SFR predictions for the volumetric SF relation in Table 2 rely on the assumption that the volume density of the outer CMZ is similar to that determined for the inner CMZ “100 pc ring”. Given the uncertainties in determining the gas density from the measured surface density, we can approach the problem from a different direction and ask, what gas densities would be required to produce the measured SFR from the measured gas masses? As shown in Table 2, the $1^\circ < l < 3.5^\circ$ region contains 0.85% of the total molecular gas in the Galaxy and 0.3% of the total SF. From Eq 8, the density of the clouds in this region should be 0.1 times the density of those in the disk, or $0.1 \times 250 \text{ cm}^{-3} \sim 25 \text{ cm}^{-3}$. This is unfeasibly low.

We conclude the column density and volumetric SF relations over-predict the SFR in the CMZ by an order of magnitude.

7 SUMMARY AND DISCUSSION

In summary, we find that the dense gas (NH_3 & $500 \mu\text{m}$) and SF activity tracers (masers & HII regions) used in this study are reliably tracing the present-day relative dense gas mass and SF activity distributions, respectively, across the Galaxy. We conclude that the striking difference between the dense gas and SF activity tracers between the GC-only and non-GC regions shows the current star formation rate per unit mass of dense gas is an order of magnitude smaller in the GC than in the rest of the Galaxy. We directly test the predictions of proposed column-density threshold and volumetric star formation relations and find, given the mass of dense gas in the GC, they over-predict the observed SFR in the GC by an order of magnitude. We conclude the current star formation relations are incomplete in some way. Any universal column/volume density relations must be a *necessary but not sufficient* condition for SF to occur.

Putting the CMZ in the context of the Galaxy as a whole, the Milky Way contains $\sim 2 \times 10^9 \text{ M}_\odot$ of gas, so the CMZ holds roughly a few percent of this. The WMAP analysis shows the CMZ also contains a few percent of the ionising photons, and hence star formation, in the Galaxy. Both the volumetric and surface density SF relations predict that a given mass of gas will form stars more rapidly if the respective densities are larger. Yet the gas in the CMZ, which has a much higher surface and volume density than any comparable mass of gas in the disk of the Milky Way, forms stars at a rate proportional to the ratio of gas in the CMZ to that in the Milky Way.

Something is required to slow the rate of SF in the CMZ compared to that in the rest of the Milky Way. An additional support mechanism, not taken into account in either the column density

threshold or volumetric SF relations, may be responsible for inhibiting the SF. One potential solution is therefore an additional term or threshold in the proposed SF relations. The most noticeable difference between clouds in the CMZ and the rest of the Milky Way, apart from the 1 to 2 order of magnitude larger volume density, is the order of magnitude larger internal cloud velocity dispersion (Morris & Serabyn 1996; Ferrière et al. 2007). We thus conclude it is likely that the relevant term is related to the additional turbulent energy in the gas providing support against gravitational collapse. A simple way to parametrise this is through the linewidth ratio, $\Delta V_{\text{ratio}} = \Delta V / \Delta V_0$, where ΔV_0 is the typical internal cloud velocity dispersion in disk molecular clouds. The Schmidt law could then be re-expressed either in terms of surface density, $\Sigma_{\text{SFR}} \propto (\Sigma_{\text{gas}})^\alpha / (\Delta V_{\text{ratio}})^b$ [$\alpha \sim 1$ to 1.4 ; $b \sim 1$], or mass of gas above the density threshold, M_{dense} , through, $\Sigma_{\text{SFR}} \propto M_{\text{dense}} / (\Delta V_{\text{ratio}})^b$. This would reconcile the star formation in the CMZ with that in the rest of the Galaxy. Theorists have wrestled with this before (e.g. Krumholz & McKee 2005; Padoan & Nordlund 2011; Krumholz et al. 2012) and we are currently seeking to test these scenarios.

However, even if the extreme environmental conditions in the CMZ do inhibit SF, they do not stop it entirely. The CMZ contains Sgr B2, one of the most extreme cluster forming regions in the Galaxy. It also contains high-mass star clusters like the Arches and Quintuplet, and at least one molecular cloud which appears to be the progenitor of such massive stellar clusters (Longmore et al. 2012; Bressert et al. 2012). Evidence exists of episodic SF events in the CMZ (Sofue & Handa 1984; Yusef-Zadeh et al. 2009; Su et al. 2010; Bland-Hawthorn & Cohen 2003) and mechanisms exist to explain how such episodic SF can occur. Gas in barred spiral galaxies like the Milky Way is funnelled from the disk through the bar to the GC (Kormendy & Kennicutt 2004; Sheth et al. 2005). If gas is continually fed from the disk to the GC, and the environmental conditions impose a higher threshold for SF to occur, the gas might build up until reaching a critical point before undergoing a burst of SF.

Although clouds near the Galactic centre in the Milky Way and other galaxies may only represent a small fractional volume of a galaxy, they can contribute a significant fraction of the total dense molecular gas. In terms of dense gas mass and environmental conditions, the Galactic centre also acts as a bridge between local SF regions in our Galaxy and SF environments in external galaxies. Understanding why such large reservoirs of dense gas deviate from commonly assumed SF relations is of fundamental importance and may help in the quest to understand SF in more extreme (dense) environments, like those found in interacting galaxies and at earlier epochs of the Universe.

REFERENCES

- Anderson L. D., Bania T. M., Balser D. S., Rood R. T., 2011, ApJS, 194, 32
 Balser D. S., Rood R. T., Bania T. M., Anderson L. D., 2011, ApJ, 738, 27
 Barnes P. J., Yonekura Y., Fukui Y., Miller A. T., Mühlegger M., Agars L. C., Miyamoto Y., Furukawa N., Papadopoulos G., Jones S. L., Hernandez A. K., O'Dougherty S. N., Tan J. C., 2011, ApJS, 196, 12
 Battersby C., Bally J., Ginsburg A., Bernard J.-P., Brunt C., Fuller G. A., Martin P., Molinari S., Mottram J., Peretto N., Testi L., Thompson M. A., 2011, A&A, 535, A128
 Beuther H., Tackenberg J., Linz H., Henning T., Schuller F., Wyrowski F., Schilke P., Menten K., Robitaille T. P., Walmsley C. M., Bronfman L., Motte F., Nguyen-Luong Q., Bontemps S., 2012, ApJ, 747, 43
 Beuther H., Walsh A. J., Longmore S. N., 2009, ApJS, 184, 366
 Bland-Hawthorn J., Cohen M., 2003, ApJ, 582, 246
 Brand J., Blitz L., 1993, A&A, 275, 67
 Bressert E., Bastian N., Evans C. J., et al 2012, A&A, 542, A49
 Bressert E., Ginsburg A., Battersby C., Bally J., Longmore S., Testi L., 2012, ArXiv e-prints
 Caswell J. L., Breen S. L., Ellingsen S. P., 2011, MNRAS, 410, 1283
 Caswell J. L., Fuller G. A., Green J. A., Avison A., Breen S. L., Ellingsen S. P., Gray M. D., Pestalozzi M. R., Quinn L., Thompson M. A., Voronkov M. A., 2011, MNRAS, 417, 1964
 Caswell J. L., Fuller G. A., Green J. A., et al 2010, MNRAS, 404, 1029
 Crocker R. M., Jones D. I., Melia F., Ott J., Protheroe R. J., 2010, Nature, 463, 65
 Danielson A. L. R., Swinbank A. M., Smail I., et al 2011, MNRAS, 410, 1687
 De Buizer J. M., Bartkiewicz A., Szymczak M., 2012, ApJ, 754, 149
 De Buizer J. M., Redman R. O., Longmore S. N., Caswell J., Feldman P. A., 2009, A&A, 493, 127
 Dunham M. K., Rosolowsky E., Evans II N. J., Cyganowski C., Urquhart J. S., 2011, ApJ, 741, 110
 Evans II N. J., 1999, ARAA, 37, 311
 Ferrière K., Gillard W., Jean P., 2007, A&A, 467, 611
 Foster J. B., Jackson J. M., Barnes P. J., Barris E., Brooks K., Cunningham M., Finn S. C., Fuller G. A., Longmore S. N., Mascoop J. L., Peretto N., Rathborne J., Sanhueza P., Schuller F., Wyrowski F., 2011, ApJS, 197, 25
 Frerking M. A., Langer W. D., Wilson R. W., 1982, ApJ, 262, 590
 Gao Y., Solomon P. M., 2004, ApJ, 606, 271
 Green J. A., Caswell J. L., Fuller G. A., Avison A., Breen S. L., Ellingsen S. P., Gray M. D., Pestalozzi M., Quinn L., Thompson M. A., Voronkov M. A., 2010, MNRAS, 409, 913
 Green J. A., Caswell J. L., Fuller G. A., Avison A., Breen S. L., Ellingsen S. P., Gray M. D., Pestalozzi M., Quinn L., Thompson M. A., Voronkov M. A., 2012, MNRAS, 420, 3108
 Hill T., Longmore S. N., Pinte C., Cunningham M. R., Burton M. G., Minier V., 2010, MNRAS, 402, 2682
 Ho P. T. P., Townes C. H., 1983, ARAA, 21, 239
 Huettemeister S., Wilson T. L., Bania T. M., Martin-Pintado J., 1993, A&A, 280, 255
 Immer K., Schuller F., Omont A., Menten K. M., 2012, A&A, 537, A121
 Jones P. A., Burton M. G., Cunningham M. R., Requena-Torres M. A., Menten K. M., Schilke P., Belloche A., Leurini S., Martín-Pintado J., Ott J., Walsh A. J., 2012, MNRAS, 419, 2961
 Kauffmann J., Pillai T., 2010, ApJL, 723, L7
 Kennicutt Jr. R. C., 1998, ApJ, 498, 541
 Kennicutt Jr R. C., Evans II N. J., 2012, ArXiv e-prints
 Kormendy J., Kennicutt Jr. R. C., 2004, ARAA, 42, 603
 Krumholz M. R., Dekel A., McKee C. F., 2012, ApJ, 745, 69
 Krumholz M. R., McKee C. F., 2005, ApJ, 630, 250
 Lada C. J., Forbrich J., Lombardi M., Alves J. F., 2012, ApJ, 745, 190
 Launhardt R., Zylka R., Mezger P. G., 2002, A&A, 384, 112
 Lee E. J., Murray N., Rahman M., 2012, ApJ, 752, 146

- Longmore S. N., Burton M. G., Barnes P. J., Wong T., Purcell C. R., Ott J., 2007, MNRAS, 379, 535
- Longmore S. N., Pillai T., Keto E., Zhang Q., Qiu K., 2011, ApJ, 726, 97
- Longmore S. N., Rathborne J., Bastian N., et al, 2012, ApJ, 746, 117
- Lumsden S. L., Hoare M. G., Oudmaijer R. D., Richards D., 2002, MNRAS, 336, 621
- Minier V., Booth R. S., Conway J. E., 2000, A&A, 362, 1093
- Minier V., Ellingsen S. P., Norris R. P., Booth R. S., 2003, A&A, 403, 1095
- Molinari S., Bally J., Noriega-Crespo A., et al. 2011, ApJL, 735, L33
- Molinari S., Swinyard B., Bally J., et al 2010, A&A, 518, L100
- Morris M., Serabyn E., 1996, ARAA, 34, 645
- Murray N., 2011, ApJ, 729, 133
- Murray N., Rahman M., 2010, ApJ, 709, 424
- Najarro F., Figer D. F., Hillier D. J., Geballe T. R., Kudritzki R. P., 2009, ApJ, 691, 1816
- Norris R. P., Byleveld S. E., Diamond P. J., Ellingsen S. P., Ferris R. H., Gough R. G., Kesteven M. J., McCulloch P. M., Phillips C. J., Reynolds J. E., Tzioumis A. K., Takahashi Y., Troup E. R., Wellington K. J., 1998, ApJ, 508, 275
- Oka T., Hasegawa T., Sato F., Tsuboi M., Miyazaki A., Sugimoto M., 2001, ApJ, 562, 348
- Onodera S., Kuno N., Tosaki T., Kohno K., Nakanishi K., Sawada T., Muraoaka K., Komugi S., Miura R., Kaneko H., Hirota A., Kawabe R., 2010, ApJL, 722, L127
- Padoan P., Nordlund Å., 2011, ApJ, 730, 40
- Peters T., Longmore S. N., Dullemond C. P., 2012, ArXiv e-prints
- Purcell C. R., Longmore S. N., Walsh A. J., Whiting M. T., et al 2012, ArXiv e-prints
- Schmidt M., 1959, ApJ, 129, 243
- Sheth K., Vogel S. N., Regan M. W., Thornley M. D., Teuben P. J., 2005, ApJ, 632, 217
- Shields J. C., Ferland G. J., 1994, ApJ, 430, 236
- Smith R. J., Longmore S., Bonnell I., 2009, MNRAS, 400, 1775
- Sofue Y., Handa T., 1984, Nature, 310, 568
- Su M., Slatyer T. R., Finkbeiner D. P., 2010, ApJ, 724, 1044
- Swinbank A. M., Smail I., et al 2010, Nature, 464, 733
- Walsh A. J., Breen S. L., Britton T., et al. 2011, MNRAS, 416, 1764
- Walsh A. J., Lo N., Burton M. G., White G. L., Purcell C. R., Longmore S. N., Phillips C. J., Brooks K. J., 2008, PASA, 25, 105
- Wu J., Evans II N. J., Gao Y., Solomon P. M., Shirley Y. L., Vanden Bout P. A., 2005, ApJL, 635, L173
- Yusef-Zadeh F., Hewitt J. W., Arendt R. G., Whitney B., Rieke G., Wardle M., Hinz J. L., Stolovy S., Lang C. C., Burton M. G., Ramirez S., 2009, ApJ, 702, 178

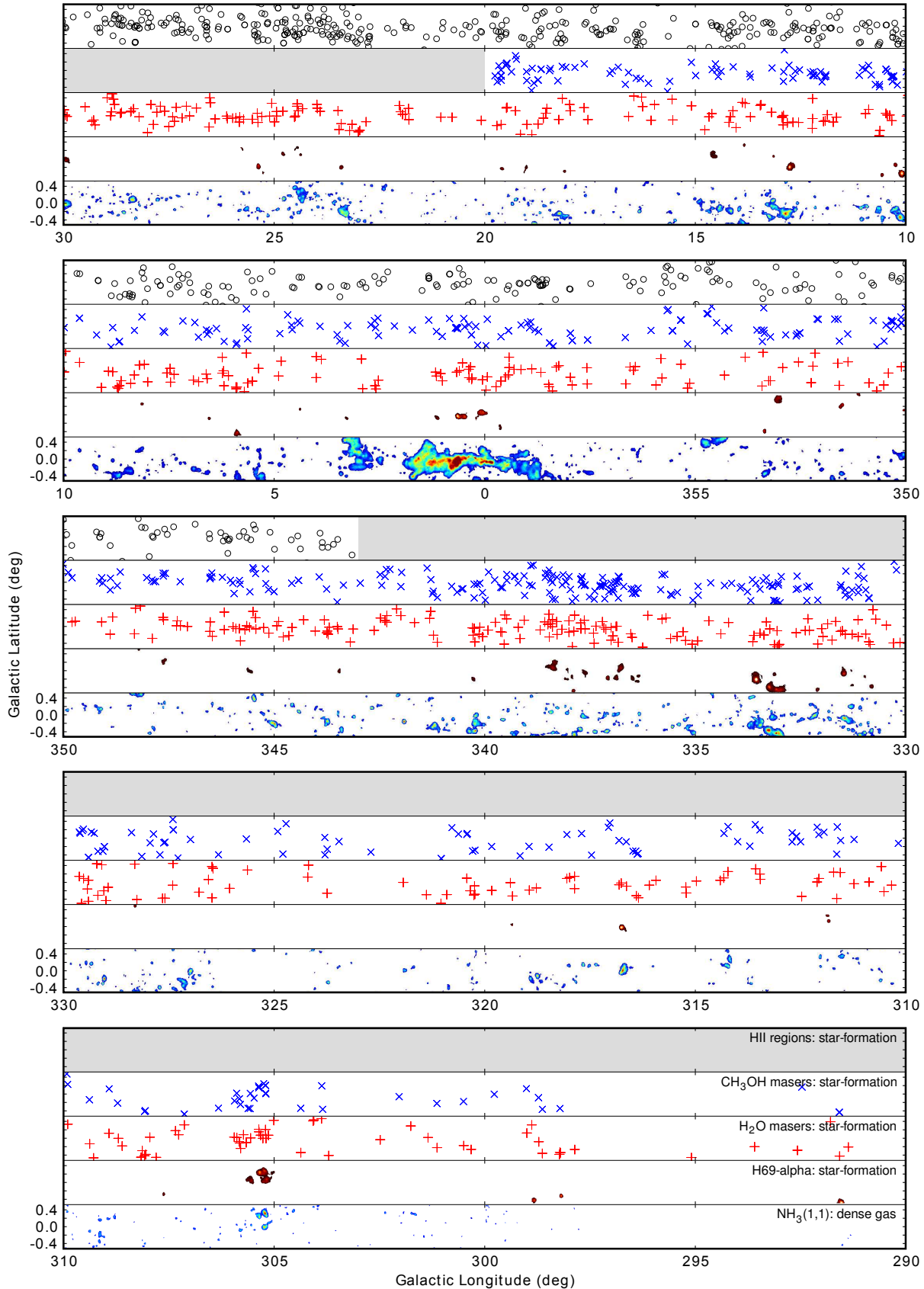


Figure 1. Distribution of dense gas and star formation activity tracers as a function of Galactic latitude and longitude. Black circles mark the positions of HII regions, blue crosses show methanol masers and red plus symbols mark water masers. Regions of sky not covered in these surveys are shaded in grey. $\text{NH}_3(1,1)$ [bottom] and $\text{H}69\alpha$ [second-bottom] integrated intensity emission is displayed using a square-root image stretch. The tracers and their function as either a dense gas or star formation activity tracer are labelled at the right hand edge of the bottom row. The central molecular zone (CMZ) can be seen as bright, extended $\text{NH}_3(1,1)$ emission from longitudes of roughly 250° to 10° .

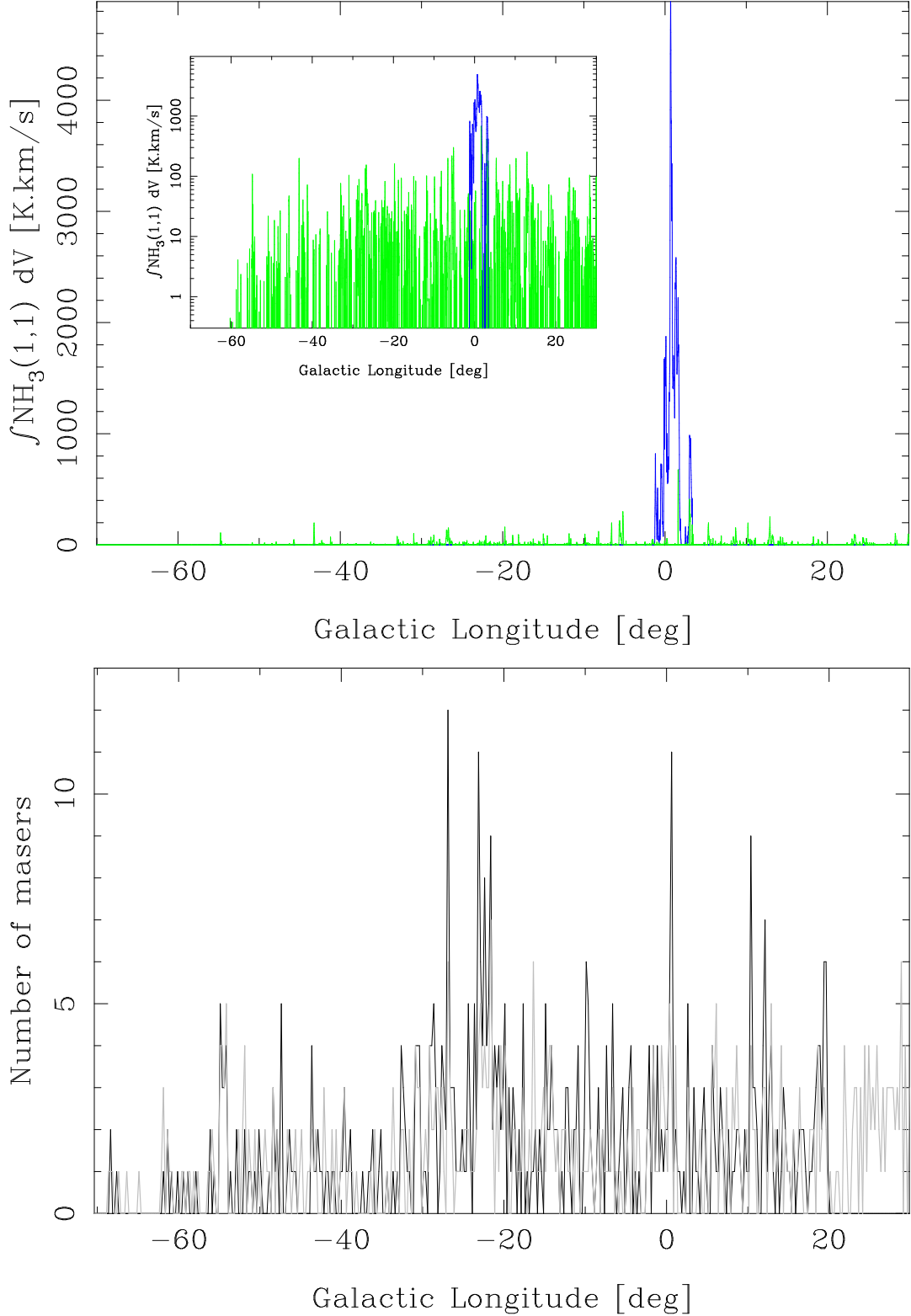


Figure 2. [Top] Dense gas distribution, traced by the $\text{NH}_3(1,1)$ integrated intensity, as a function of Galactic longitude ($2'$ bins). The emission was split into two regions: a Galactic centre region encompassing the central molecular zone (blue) and the rest of the Galaxy (green). The Galactic centre region clearly dominates, accounting for $\sim 80\%$ of the $\text{NH}_3(1,1)$ integrated intensity emission, despite only accounting for $\sim 4\%$ of the total survey area. The inset shows the same plot but with a logarithmic scale on the y-axis. [Bottom] Star formation activity, traced by the number of water masers (grey) and methanol masers (black; data for $l > 20^\circ$ unavailable), as a function of Galactic longitude (0.25° bins). In comparison to the $\text{NH}_3(1,1)$ emission, the distribution of both maser species is relatively flat with Galactic longitude.

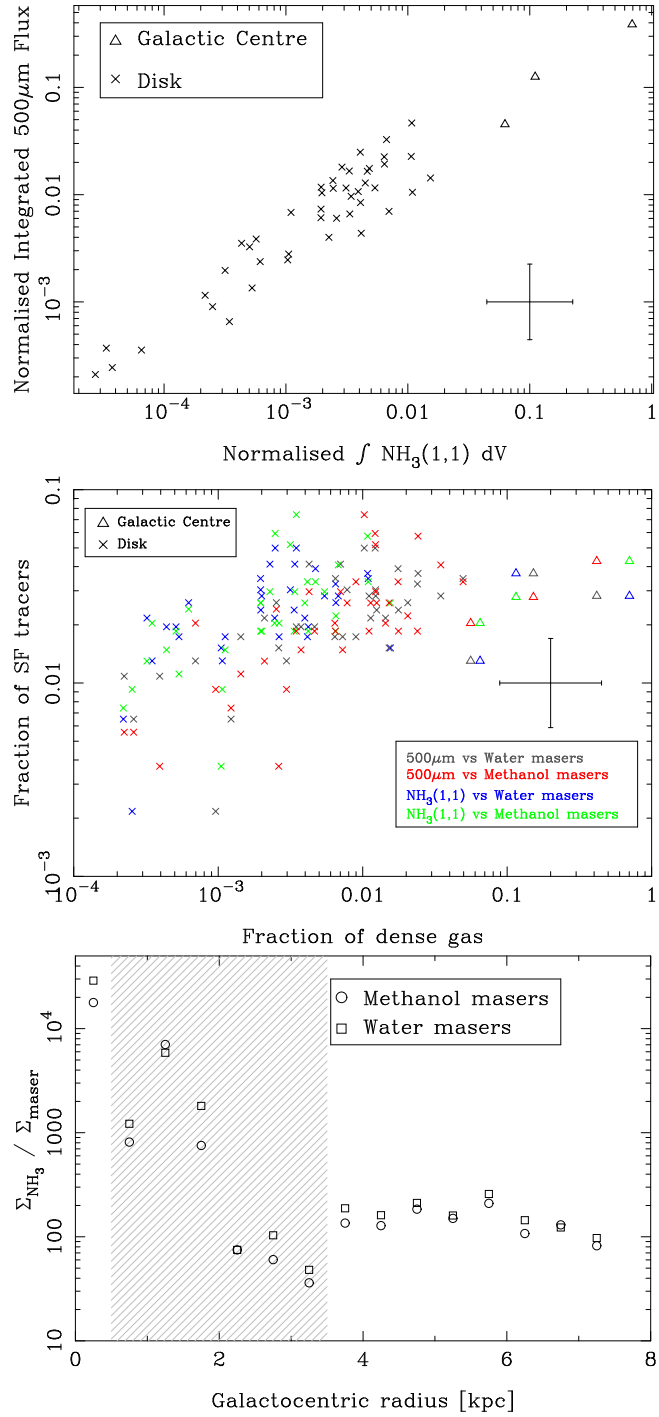


Figure 3. [Top] Comparison of two independent dense gas tracers, NH₃(1,1) integrated intensity vs. the integrated 500 μm flux, for each 2° longitude bin (normalised to the total flux in that tracer). [Middle] The fraction of dense gas tracers (NH₃(1,1) integrated intensity and 500 μm flux) vs fraction of star formation tracers (water and methanol masers) for each 2° longitude bin between $-70^\circ < l < 20^\circ$ (the mutually-overlapping coverage of MMB and HOPS). Different colours show different combinations of dense gas and SF tracers. In both top and middle plots, the Galactic centre (GC-only) and disk (non-GC) regions are shown as triangles and crosses, respectively. Representative uncertainties of a factor 5 in dense gas mass and 3 in maser counts are shown as error bars. [Bottom] Ratio of dense gas surface density (NH₃(1,1) integrated intensity) to star formation surface density (methanol and water masers) as a function of Galacto-centric radius, R_{GC}. The hatched region shows the radial range over which the rotation curve used to derive R_{GC} is unreliable. The surface density ratios over this region should be ignored.

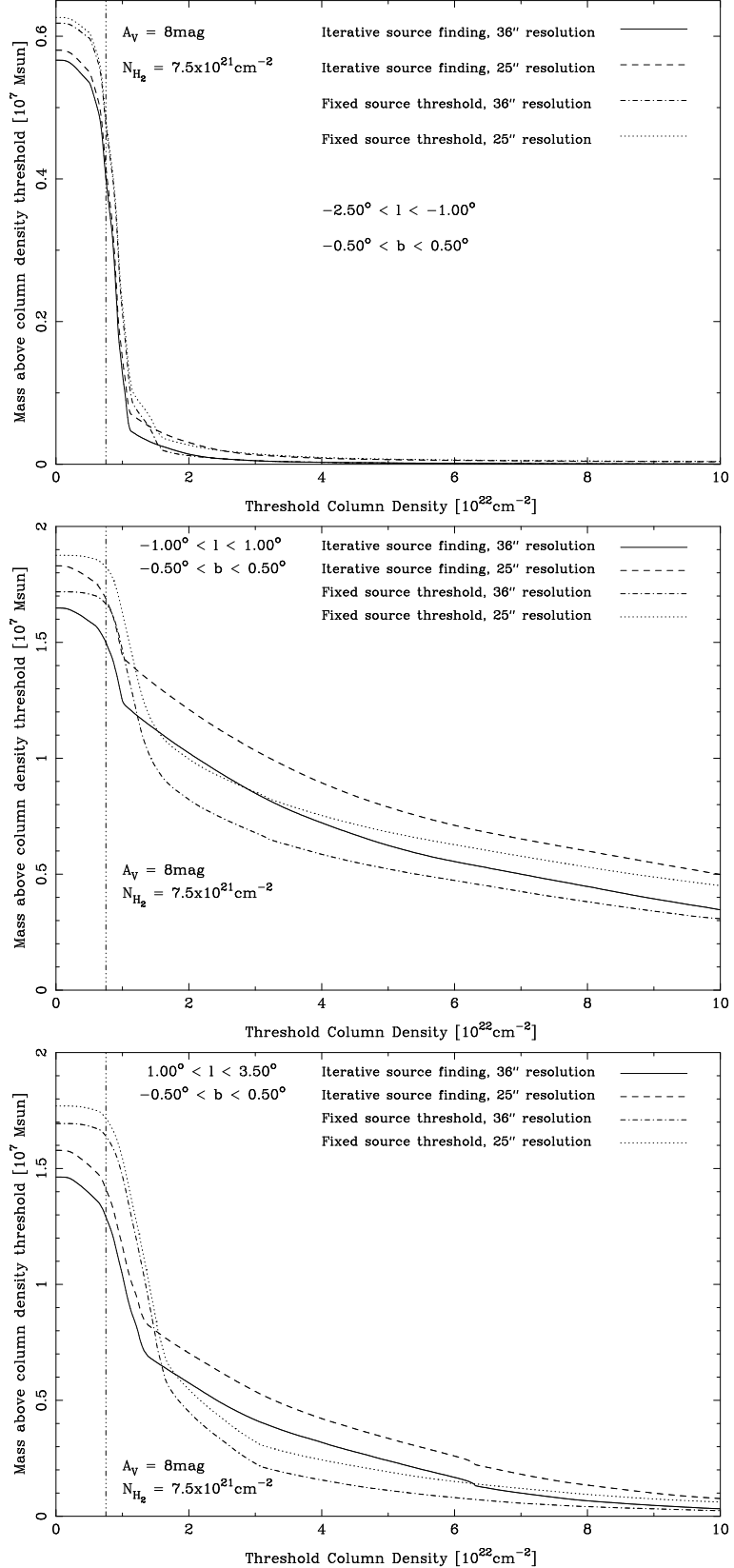


Figure 4. Total mass in various longitude ranges of the CMZ which lies above a range of column density thresholds. The vertical dashed line shows the proposed column density threshold of $7.5 \times 10^{21} \text{ cm}^{-2}$, calculated from the extinction threshold of $A_V = 8 \text{ mag}$ and assuming an $A_V \rightarrow N_{H_2}$ conversion of $N_{H_2} = A_V \times 0.95 \times 10^{21} \text{ cm}^{-2}$. The different curves show the effect on the derived column density of using different wavelength bands and different source-extraction algorithms. From this we conclude the column densities are robust to the 10-20% level.

Table 1. Properties of the Galactic plane surveys used in this work.

Survey	Angular Resolution	Transition or Continuum	Frequency or wavelength	l_{min}	l_{max}	b_{min}	b_{max}	Notes
GBT HRDS	82''	H86 α –H93 α	9 GHz	-17°	67°	-1°	1°	Targetted HII region survey
HOPS	2'	NH ₃ (1,1)	23.4 GHz	-70°	30°	-0.5°	0.5°	$n_{crit} \sim 10^{3-4} \text{ cm}^{-3}$
HOPS	2'	Water maser	22 GHz	-70°	30°	-0.5°	0.5°	Traces SF activity
HOPS	2'	H68 α	22 GHz	-70°	30°	-0.5°	0.5°	Traces HII regions
MMB	~1''	Methanol maser	6.7 GHz	-180°	20°	-2°	2°	Traces SF activity
Hi-GAL	35''	continuum	70,160,250, 350,500 μm	-60°	60°	-1°	1°	optically-thin dust emission ($S_\nu \propto M_{gas}^{dense}$)

Table 2. Gas mass and ionising photon rate (Q) for various longitude and latitude ranges of the CMZ. The second row corresponds roughly to the longitude range for the inner ~ 150 pc of the CMZ. The first and third rows correspond roughly to the longitude ranges of the outer ~ 150 to ~ 500 pc of the CMZ, in the negative and positive longitude ranges, respectively. The gas masses are derived from the HiGAL column density maps. The value in column 5 is the total mass in that longitude and latitude range, whereas column 6 reports the mass above the column density threshold corresponding to an extinction of $A_V = 8$ mag (see text for details). The range in values in column 7 corresponds to the total Q assuming near and far kinematic distances, respectively (Lee et al. 2012). Column 8 gives the fraction (in percent) of the total Galactic molecular gas contained in column 5, assuming a total Galactic molecular gas mass of $2 \times 10^9 M_\odot$. Column 9 gives the fraction (in percent) of the total Galactic Q of $2.9 \times 10^{53} \text{ s}^{-1}$ (Lee et al. 2012). Column 10 gives the corresponding SFRs for each of the regions. The values in parentheses in columns 7, 9 and 10 are the Q values over the same longitude regions if the latitude range is doubled to $|b| < 1^\circ$. Only the $|l| < 1^\circ$ longitude range is affected. The SFRs in columns 11 and 12 are those predicted from the column density threshold and volumetric SF relations, respectively (see text for details).

b_{min} (deg)	b_{max} (deg)	l_{min} (deg)	l_{max} (deg)	mass ($10^7 M_\odot$)	mass _{$A_V \geq 8$} ($10^7 M_\odot$)	Q (10^{51} s^{-1})	mass/ M_{TOT} (%)	Q/Q _{TOT} (%)	SFR _Q ($M_\odot \text{ yr}^{-1}$)	SFR _{$A_V \geq 8$} ($M_\odot \text{ yr}^{-1}$)	SFR _{ρ} ($M_\odot \text{ yr}^{-1}$)
-0.5	0.5	-2.5	-1.0	0.6	0.4	2–6	0.3	1.3	0.016	0.184	0.14
-0.5	0.5	-1	1	1.8	1.7	3–4(13)	0.9	1.2(4.5)	0.012–0.018(0.06)	0.782	0.41
-0.5	0.5	1	3.5	1.7	1.6	0.1–2	0.85	0.3	0.0036	0.736	0.39

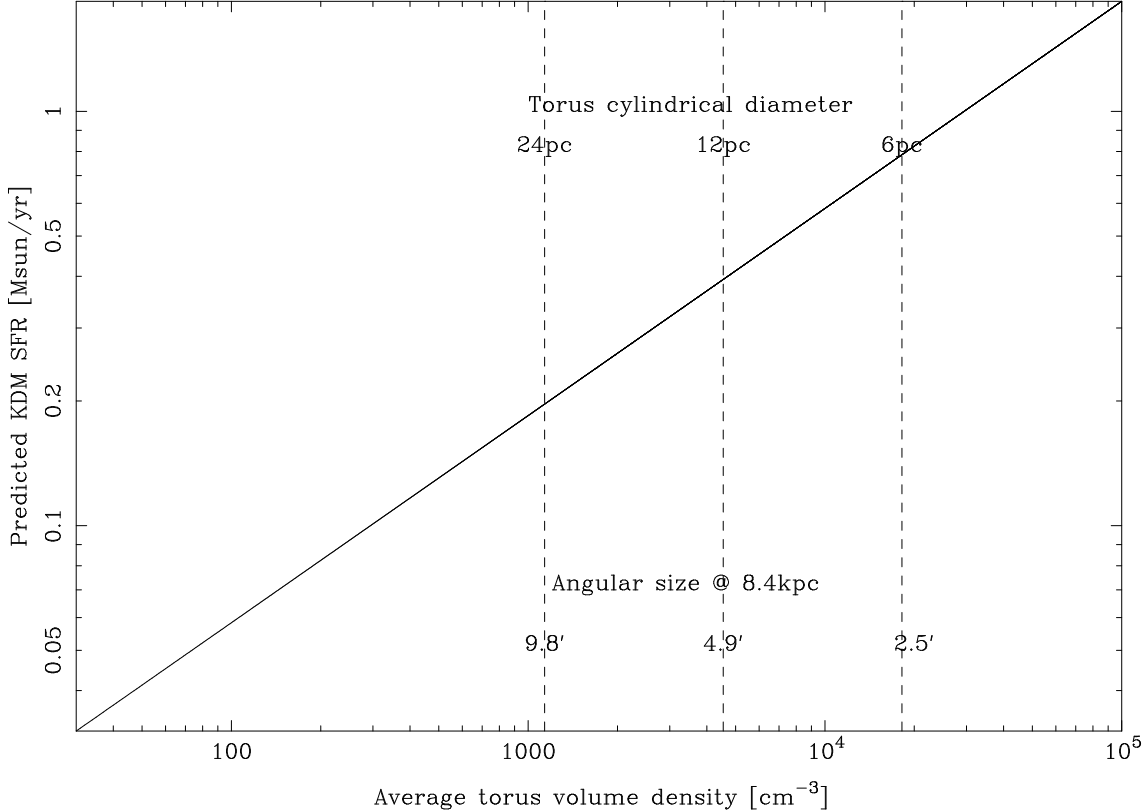


Figure 5. The predicted star formation rate from the Krumholz et al. (2012) volumetric relation as a function of the average gas volume density. The dashed vertical lines show the average volume density assuming the $1.8 \times 10^7 M_{\odot}$ of gas in the region $|l| < 1^\circ$, $|b| < 0.5^\circ$ (see Table 2) lies in a cylindrical ring with semi-major and semi-minor axes of 100 pc and 60 pc, respectively, with the diameter specified by the annotation for each line. The observed thickness (and hence the inferred diameter) of the ring varies from ~ 6 pc to factors of several larger. We estimate the average volume density to be $\sim 5 \times 10^3 \text{ cm}^{-3}$, with a corresponding predicted SFR of $\sim 0.4 M_{\odot}/\text{yr}$.

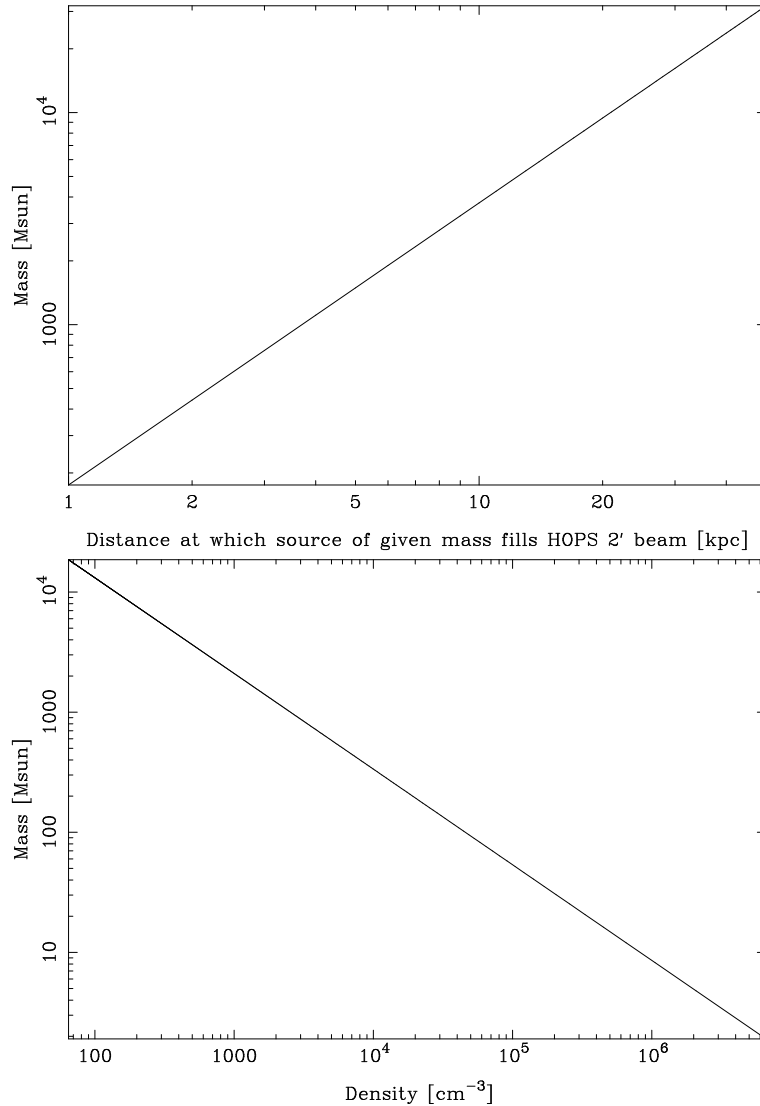


Figure 6. [Top] Estimating the distance at which molecular clouds of a given mass will be the same angular size as the 2' HOPS beam. The physical radius as a function of mass was estimated using the Kauffmann & Pillai (2010) empirical mass-size relationship for molecular clouds which will proceed to form high mass stars. The line in the plot shows the distance at which a molecular cloud of that mass will have an angular size of 2'. Molecular clouds below the line will suffer from beam dilution so the observed surface brightness, and therefore integrated intensity, will be reduced. Molecular clouds above this line will not suffer from this affect. [Bottom] Density of clouds as a function of their mass, calculated from the Kauffmann & Pillai (2010) empirical mass-size relationship.